Sheffield Hallam University

Alternative reductants for foam control during vitrification of high-iron High Level Waste (HLW) feeds

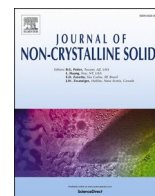RIGBY, Jessica, DIXON, Derek, KLOUZEK, Jaroslav, POKORNY, Richard, THOMPSON, Paul, SCRIMSHIRE, Alex <http://orcid.org/0000-0002-6828-3620>, KRUGER, Albert, BELL, Anthony <http://orcid.org/0000-0001-5038-5621> and BINGHAM, Paul <http://orcid.org/0000-0001-6017-0798>

Available from Sheffield Hallam University Research Archive (SHURA) at:

https://shura.shu.ac.uk/31558/

Citation:

Alternative reductants for foam control during vitrification of high-iron High Level Waste (HLW) feeds

J.C. Rigby [a,*], D.R. Dixon [b], J. Kloužek [c,d], R. Pokorný [c,d], P.B.J. Thompson [e], A. Scrimshire [a], A.A. Kruger [f], A.M.T. Bell [a], P.A. Bingham [a]

[a] Materials and Engineering Research Institute, College of Business, Technology and Engineering, Sheffield Hallam University, City Campus, Howard Street, Sheffield S1 1WB, United Kingdom
[b] Pacific Northwest National Laboratory, Richland, WA 99354, United States
[c] University of Chemistry and Technology Prague, Technicka 5/1905, 166 28 Prague 6, Czechia
[d] Institute of Rock Structure and Mechanics of the Czech Academy of Sciences, V Holesovickach 41, 182 09 Prague 8, Czechia
[e] XMaS UK CRG Beamline, ESRF - The European Synchrotron, 71, avenue des Martyrs, 38000 Grenoble, France
[f] U.S. Department of Energy, Office of River Protection, Richland, WA 99352, United States

ARTICLE INFO

ABSTRACT

Foaming during vitrification of radioactive waste in Joule-Heated Ceramic Melters (JHCM) is exacerbated by trapping of evolving gases, such as CO_2, NO_x and O_2, beneath a viscous reaction layer. Foaming restricts heat transfer during melting. Sucrose is employed as the baseline additive at the Hanford site in Washington State, USA to reduce foaming. Alternative carbon-based reductant additives were explored in simulated, inactive Hanford high-iron HLW-NG-Fe2 feeds, for both their effect on foaming and to give insight to the behaviour of multivalent species in glass melts under different redox conditions. Graphite, coke (93% C), formic acid and HEDTA additives were compared with sucrose, and a feed with no additive. Graphite and coke additions proved most effective in reducing the maximum foam volume by $51 \pm 3\%$ and $54 \pm 2\%$, respectively, compared with $24 \pm 5\%$ for sucrose. Lower foaming could result in more efficient vitrification in JHCMs. Reductants also affected redox ratios in the multivalent species present in the feed. The order of reduction, $Mn^{3+}/Mn^{2+} > Cr^{6+}/Cr^{3+} > Ce^{3+}/Ce^{4+} > Fe^{3+}/Fe^{2+}$ was as predicted on the basis of their redox potentials. There is less reduction overall, particularly in the $Fe^{3+} \rightarrow Fe^{2+}$, than predicted by the calculations, attributed to the oxygenated atmosphere of the experiments.

1. Introduction

The Hanford site in Washington State, USA, is home to ~200,000 m³ of radioactive legacy waste, historically stored in 177 carbon-steel tanks underground [1–3]. The Waste Treatment & Immobilization Plant (WTP) located at Hanford is currently under construction and commissioning. The tank waste will be partitioned into low-activity waste (LAW) and high-activity fractions which will then be vitrified in Joule-Heated Ceramic Melters (JHCM) [4–6] in separate LAW and high-level waste (HLW) vitrification facilities, respectively. The plan for the first phase of treatment is named Direct Feed LAW (DFLAW). Once LAW sustained operations are underway efforts will turn to HLW vitrification. The waste will be mixed with glass forming chemicals (GFCs) and fed to the melter. After feeding the melter, the liquid slurry lands on top of the melt pool creating a feed reaction layer called the "cold cap" [7]. At the bottom of the cold cap, glass-forming melt produced in the later stages of the conversion process can trap gases that are evolving during the feed-to-glass reactions, causing foaming. Foaming can insulate the melt pool, reducing heat transfer to the reacting material [8–10] and thereby reducing the efficiency of the process. In extreme cases, foaming can pose a risk to melter components [11].

Feeds that are rich in nitrates generally cause excessive foaming, as the nitrates release gases in the 600–800 °C temperature range, the same range as when the viscous glass-forming melt is evolving [12,13]. The foam that forms in this temperature range is referred to as *primary foam* [4,5,14] and is caused by the evolution of NO_x and CO_2 from batch nitrates, organics, and carbonates, as well as smaller contributions from O_2 and SO_2. At higher temperatures, the NO_x and CO_2 evolutions are

completed, while the contributions from O_2 and SO_2 increase, as these gases are usually released up to the melting temperature of the glass, ~1150 ℃ [2,4] provoked by redox reactions [12,13,15]. Foaming at higher temperatures, once primary foam has collapsed, is referred to as *secondary foaming* [5,8,9,12]. Compared to LAW feeds, secondary foaming is much more prevalent in vitrification of HLW streams that are rich in multivalent species such as Fe_2O_3, Cr_2O_3 and MnO_2 [12,15,16].

The high-iron inactive simulated feed, HLW-NG-Fe2, Table 1, developed by Vitreous State Laboratory of The Catholic University of America (VSL), Washington DC [11], is of particular interest for exploring the foaming behaviour of HLW feeds as it foams up to 10 times its original volume during heating [2,17]. This was examined by pellet expansion tests where a feed pellet was heated to 1150 ℃ at 10 ℃ min^{-1} and photographs are taken at temperature intervals to track the volume expansion [6,7].

Sucrose is the baseline reductant additive at the Hanford site. This choice, for balancing the C/N ratios in feeds was selected based on experience at the defense Waste Processing Facility (DWPF), SC, West Valley Demonstration Project, NY and Hanford Low-Activity Waste feed research [12,18–20]. In the early evaluation of different reductants on the Hanford site waste glasses, particularly using carboxylic acids, the effect on redox behaviour of mixed multivalent species in feeds was not well understood [21]. In 1995, Seymour suggested that fine tuning of the interrelationship of the complex redox chemistry of the cold cap and melt pool should be pursued [21]. Previous studies relating directly to Hanford LAW compositions have explored the effects of sucrose and formic acid on the redox behaviour of waste glasses [5,19,22,23]. A study varying the carbonate and nitrate content of the high-iron HLW-NG-Fe2 feed concluded that the previous algorithms used to determine the amount of sucrose to add to high-nitrate LAW feeds needs to be modified for HLW feeds high in multivalent species such as Fe to avoid overreduction, and further testing is required to better define the relationship between sources of carbon [24]. Experiments studying coke and other reductant additions to industrial soda-lime-silica type glass batches to promote sulphate decomposition (thereby helping decrease foam generation) have also measured iron redox previously [25–27]. Two studies reported reduction in Fe and melt oxygen partial pressure in commercial glasses using graphite addition [27,28]. Beyond the suggestion of its use in 1995 [29], the effects of HEDTA on glass redox has not been explored in commercial glasses or waste glasses, despite it being present in some Hanford waste streams [30–33].

The reductants selected provide a wide range of carbon content values per gram of compound, Table 2 [29]. To our knowledge, little research has been published on reductant additions in Hanford HLW feeds, where, in particularly high-foaming feeds such as the HLW-NG-Fe2 feed [7], there is opportunity for increased processing

Table 1
HLW-NG-Fe2 composition developed by the Vitreous State Laboratory of The Catholic University of America (VSL) to immobilise the C-106/AY-102 high-iron tank waste, adapted from [11].

Raw Material	Batch g/100 g (glass)	Raw Material	Batch g /100 g (glass)
$Al(OH)_3$	8.61	$Ni(OH)_2$	0.59
H_3BO_3	0.56	$FePO_4 \cdot 2H_2O$	1.71
$Na_2B_4O_7 \cdot 10H_2O$	37.16	PbO	0.63
$CaCO_3$	0.94	Na_2SiO_3	8.03
CeO_2	0.12	Na_2SO_4	0.39
$Cr_2O_3 \cdot 1.5H_2O$	0.30	SiO_2	37.33
$Fe(OH)_3$	20.54	$SrCO_3$	0.28
$La(OH)_3$	0.11	ZnO	0.03
Li_2CO_3	3.87	Zr $(OH)_4 \cdot 0.654H_2O$	1.57
$Mg(OH)_2$	0.24	$NaNO_2$	0.01
MnO_2	3.98	$NaNO_3$	0.45
NaOH	0.81	$H_2C_2O_4 \cdot 2H_2O$	0.06
Na_2CO_3	4.04	Total	132.36

Table 2
Reductants used for each of the feeds studied and the associated carbon g^{-1} per compound [29].

Feed Name	Reductant Carbon Source	Carbon content /g of reductant
HLW-NG-Fe2-S	Sucrose ($C_{12}H_{22}O_{11}$)	0.42
HLW-NG-Fe2-G	Graphite (C)	1.0
HLW-NG-Fe2-C	Coke Dust (93% C)	0.93
HLW-NG-Fe2-F	Formic Acid (CH_2O_2)	0.26
HLW-NG-Fe2-H	HEDTA* ($C_{10}H_{18}N_2O_7$)	0.43

* N'(-2 hydroxyethyl) ethylenediamine-NNN' triacetic acid.

efficiency. In addition, wider understanding of the effects of chemically different reductants in radioactive waste feed vitrification can also add to the pool of knowledge in the field. The aims of this study were thus to: (a) determine the effect of alternative reductants on the foaming behaviour of simulated HLW-NG-Fe2 feed; and (b) contribute to the pool of knowledge on the effects of alternative reductants in radioactive waste feed vitrification and glass melting. We also consider the behaviour of the multivalent species in the feed, comparing those to work by Schreiber [34–36] to understand the influence of different reductants on the redox behaviour of these species and the oxygen fugacity, fO_2, in the melt.

The coke used in the sample is ~93.3 wt% C according to x-ray fluorescence (XRF), with 3.1 wt% O, 1.1 wt% Si, 0.8 wt% Al, 0.6 wt% Fe, 0.4 wt% S, 0.3 wt% Ca, 0.1 wt% Mg and 0.1 wt% Ti, with trace amounts of P, Na, Cl, Ba, Sr, Mn, Cr, Ru and Ni. The mechanisms of foam expansion and collapse are determined by the quantity of gas evolution, the temperature of gas evolution and the viscosity of the melt at the temperatures of gas evolution [6,37,38]. The secondary foam, caused by SO_2 and O_2 evolution is less significant than the residual CO_2 contributing to the primary foam for most feeds. The HLW-NG-Fe2 feed has been described as exhibiting irregular foaming with multiple secondary peaks prior to foam collapse [6,7]. The HLW-NG-Fe2 feed has been shown to produce more oxygen than regular feeds, as a result of Fe^{3+} reducing to Fe^{2+} [7].

The order of reduction of multivalent species, *M*, in the same melt and temperature conditions has been derived by Schreiber and colleagues [35,39] and is correlated to assigned relative electron reduction potentials, E_M^* [39], given by:

$$-\log(fO_2) = \frac{4}{n}\log\left[\frac{M^{(m-n)+}}{M^{m+}}\right] + E_M^*. \quad (1)$$

where *n*, is the number of transferred electrons in the redox reaction $M^{(m-n)+} \leftrightarrow M^{m+}$. The relative electron reduction potentials provide the order in which each multivalent species will reduce in a glass melt. For those in the HLW-NG-Fe2 glass, the order of $Mn^{3+}/Mn^{2+} > Cr^{6+}/Cr^{3+} > Ce^{3+}/Ce^{4+} > Fe^{3+}/Fe^{2+}$ is expected based on the electromotive force series defined by Schreiber [39–44]. These electron reduction potentials have been used in many studies of glass melting to predict the redox behaviour, those of interest to this study are presented in Table 3 [36,41, 44,45]. The range of reductants explored in this study provide an

Table 3
Relative reduction potentials for redox states of key multivalent species in the HLW-NG-Fe2 feed for a borosilicate melt at 1150 ℃ [39].

Element	Initial Oxidation State	Final Oxidation State	Reduction Potential
Chromium	Cr^{3+}	Cr^{2+}	-1.38
	Cr^{6+}	Cr^{3+}	-0.04
Cerium	Ce^{4+}	Ce^{3+}	-0.03
Iron	$Fe2+$	$Fe0$	-1.27
	Fe^{3+}	Fe^{2+}	-0.68
Manganese	Mn^{3+}	Mn^{2+}	0.33
Nickel	Ni^{2+}	Ni^0	-1.06
	Ni^{3+}	Ni^{2+}	0.69

interesting case for exploring the redox behaviour of multiple multivalent species in glasses melted under different redox conditions.

2. Experimental methods

2.1. Sample preparation

Feeds based on the composition in Table 1 were batched on a 2 d p. scale with >99% purity raw materials. Chemicals were mixed with deionised water with a target glass yield of 290 g L^{-1} and stirred continuously during batching. Reductants, Table 2, were added to the feed slurries during mixing to ensure homogeneity. The feeds were then dried at 105 ℃ for 24 h. Twenty grams of dried feeds were heated in a refractory-lined induction furnace up to 600, 800, 1000 and 1150 ℃ at 10 ℃ min^{-1} and quenched in air.

A preliminary study investigated 0, 0.5, 1, 2, 3, 4, 5 and 6 wt% of graphite additions to the HLW-NG-Fe2 feed, with graphite having the highest carbon content per gramme. Feeds were melted in a refractory lined induction furnace at 1150 ℃. X-ray powder diffraction (XRD) was performed on a PANalytical X'Pert Pro-X-ray powder diffractometer, using Cu Kα X-rays (λ = 1.5406 Å) with a power setting of 40 mA / 40 kV. Samples were spun during data collection to improve the powder average. XRD scans were collected over the angular range 5 to 80 ° 2θ. From the positions of the Bragg reflections in the XRD scans crystalline phases were identified using the PANalytical HighScore Plus software and the International Centre for Diffraction Data (ICDD) Powder Diffraction File database [46]. The XRD patterns are given in Appendix A. A spinel phase was present in all samples. At 5 and 6 wt% graphite addition, a peak emerged ~45 ° 2θ which is close to the main peak in this angular range for metallic Fe (ICDD Powder Diffraction File ref. 6–696), at 44.674 ° 2θ, however, without further peaks to assign to the phase the presence of metallic iron cannot be confirmed. To avoid excessive crystallinity or precipitation of any metallic phases [19], 3 wt% additions of each reductant were chosen for this study.

2.2. Thermal analysis

For feed volume expansion tests (FETs), 13 mm diameter pellets of dried feed, pressed under 10 T for 3 min, were heated at 10 ℃ min^{-1} to 1150 ℃ in an electric furnace with an observation port. Photographs were taken at ~100 ℃ intervals initially, and then at 20 ℃ intervals, once the pellets began to change shape, and analysed for the volume (assuming spherical symmetry) in Photoshop®. The volume was then normalised to the volume of the final glass, calculated using the pellet mass, density and loss on ignition. Averages of three runs were taken for each composition.

The release rate of evolved gases (EGA) was measured using a gas chromatograph and Agilent 6890/5973 N mass spectrometric detector. The equipment was connected to a silica tube inside a furnace containing each sample. The furnace heated the sample to 1150 ℃ at 10 ℃ min^{-1} under He, flowing at 50 ml min^{-1}.

Thermogravimetric Analysis (TGA) was performed on a TA Instruments SDT 650 DSC/TGA. Samples were heated in N_2, from 30 – 1150 ℃ and held at 1150 ℃ for 10 min. Processing of the spectra was performed in the TRIOS® and Origin Pro® software packages.

2.3. X-ray fluorescence spectroscopy

For compositional analysis of the coke sample, the coke was mixed thoroughly with cellulose binder at a ratio of 4:1 sample to binder. The mixture was placed in an aluminium mould in the Retsch PP 40. The pellet was pressed for 60 s hold time under 20 T. The pressed pellet was then sent for XRF at Glass Technology services, Sheffield, UK. XRF was performed on a Bruker S4 pioneer – 3 kW wavelength dispersive X-ray fluorescence spectrometer with a rhodium X-ray tube.

2.4. X-ray diffraction and phase identification

X-ray diffraction was performed as described in Section 2.1, on the feed samples heated to 600, 800, 1000 and 1150 ℃, and phase ID and refinement of XRD patterns carried out using the ICDD and Rietveld refinement functions in the HighScore Plus software [47,48]. Addition of 5 wt% Si to each ground sample was used to determine the amorphous content, and therefore the quantitative proportion of each phase,

2.5. X-ray absorption near-edge spectroscopy (XANES)

Samples of each of the feeds heat treated at 600, 800, 1000 and 1150 ℃ were analysed using X-ray Absorption Near-Edge Spectroscopy for the behaviour of Cr, Ce, and Mn during melting. Pressed pellets were prepared of powdered samples mixed with cellulose acetate at appropriate ratios to form sample 10 mm diameter, ~0.5 mm thick. K-edge spectra of Cr, and Mn were collected and the Ce L$_{III}$-edge. The Ni K-edge was also collected but there was no observed change in the edge at the resolution attainable. It is assumed based on the lack of apparent change, and the reduction potential of Ni that the oxidation state does not change throughout melting [39]. All HLW-NG-Fe2, HLW-NG-Fe2-S and -G samples were measured on the BM28 XMaS beamline [49] at the European Synchrotron Radiation Facility (ESRF), France, and HLW-NG-Fe2-C, -F and -H samples were measured at the B18 XAS beamline [50] at the Diamond Light Source, UK. Both beamlines operated with a Si monochromator and an energy range greater than that required for all edges measured.

All spectra were collected in simultaneous fluorescence and transmission mode. Only Mn was present in the samples in sufficient quantities to obtain useful transmission data. Spectra were collected from energies ~150 eV below the absorption edge and up to 250 eV beyond the edge. Data intervals of 0.15 eV over the pre-edge features was attainable at the BM28 beamline at ESRF and steps of 2 eV were used before and after the edge. At the B18 beamline at Diamond, 0.3 eV steps were used for the entire spectra. Up to 5 repeat measurements were performed at the BM28 beamline at ESRF and up to 20 repeat measurements were performed at the B18 beamline at Diamond, improving signal to noise ratios. Reference materials for each likely oxidation state were measured at each beamline, Cr_2O_3 (Cr^{3+}), $Na_2Cr_2O_7$ (Cr^{6+}), Mn-foil, MnO (Mn^{2+}), MnO_2 (Mn^{4+}), Mn_2O_3 (Mn^{3+}), CeO_2 (Ce^{4+}), $Ce_2(C_2O_4)_3$ (Ce^{3+}). Spectra were processed with the Athena software (0.9.26) [51] where scans were deglitched, normalised and merged. The integrated self-absorption correction was applied to the fluorescence spectra of the Mn K-edge. Measurements of redox states of multivalent species were taken on quenched samples, under the assumption that no changes to the redox states occurs during cooling. Studies show that these measurements may vary by up to 20% when compared to high-temperature measurements [43].

2.6. ^{57}Fe Mössbauer spectroscopy

For analysis of the redox state of the iron in the final glasses, samples heated to 1150 ℃ for each of the feeds were powdered for room temperature ^{57}Fe Mössbauer spectroscopy. The 14.4 keV γ-rays from decay of a 25 mCi ^{57}Co source in a Rh matrix oscillated at constant acceleration, were absorbed by the sample. ^{57}Fe Mössbauer spectra were collected in the velocity range of ±12 mm s^{-1} relative to α-Fe. Signal to noise was improved with collection times of up to two weeks. The Recoil software package was used to fit the data, and the assumption was made that the recoil-free fraction ratio $f(Fe^{3+}/Fe^{2+}) = 1.0$ when obtaining redox ratios from fitted component area ratios. Each of the spectra were fitted with Lorentzian doublets and sextets for the paramagnetic and magnetic contributions, respectively.
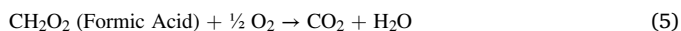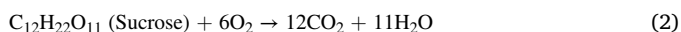
3. Results

3.1. Feed volume expansion testing

Feed expansion tests, illustrated in Fig. 1, show the range of foaming behaviours of the feeds with the 5 different reductants added at 3 wt%, compared with the original feed with no reductants. While adding sucrose has a reducing effect on the maximum foam volume, similar to that of adding HEDTA, graphite and coke have a significantly greater effect. The maximum normalised foam volume is linear with the carbon content per gram of reductant added, shown in Fig. 2. Table 4 shows the reduction in maximum foam volume, correlates reasonably well with the reductant equivalence per gram of compound.

3.2. Gas evolution

The following decomposition reactions for the reductants assume that oxygen is available such that all C evolves as CO_2 and all N as NO,

$$C_{12}H_{22}O_{11} \text{ (Sucrose)} + 6O_2 \rightarrow 12CO_2 + 11H_2O \qquad (2)$$

$$C \text{ (Graphite)} + O_2 \rightarrow CO_2 \qquad (3)$$

$$0.93C \text{ (Coke)} + 0.93O_2 \rightarrow 0.93CO_2 \qquad (4)$$

$$CH_2O_2 \text{ (Formic Acid)} + \tfrac{1}{2} O_2 \rightarrow CO_2 + H_2O \qquad (5)$$

$$C_{10}H_{18}N_2O_7 \text{ (HEDTA)} + 12O_2 \rightarrow 10CO_2 + 9H_2O + 2NO \qquad (6)$$

These equations are used in this section to compare the measured gases evolved by EGA with the expected gas evolution. The derivative of the measured mass changes during heating by TGA of sucrose, graphite, coke and HEDTA, in isolation, are given in the top graph in Fig. 3, providing the temperatures of gases evolved. No measurements were taken on pure formic acid due to potential damage to the equipment.

Most gas evolution, therefore, decomposition, of the sucrose and HEDTA samples occurs prior to 500 ℃. Minimal gas evolution from coke or graphite was detected within the temperature range measured. The same experiment was performed on the HLW-NG-Fe2 feed with the added reductants, the bottom graph in Fig. 3. Gas evolution peaks in the range 200–600 ℃ are similar for the HLW-NG-Fe2 and HLW-NG-Fe-2-G and C feeds. Variation in behaviour prior to 600 ℃ in the HLW-NG-Fe2-S, F and H feeds can be attributed to decomposition reactions, in Eqs. (2), (5) and (6). In the bottom graph in Fig. 3, the HLW-NG-Fe2-G feed has a mass loss event starting ~1050 ℃, which absent in the above graph. This indicates that the graphite decomposes prior to 1150 ℃ in the glass melt, but does not decompose in this temperature range in air.

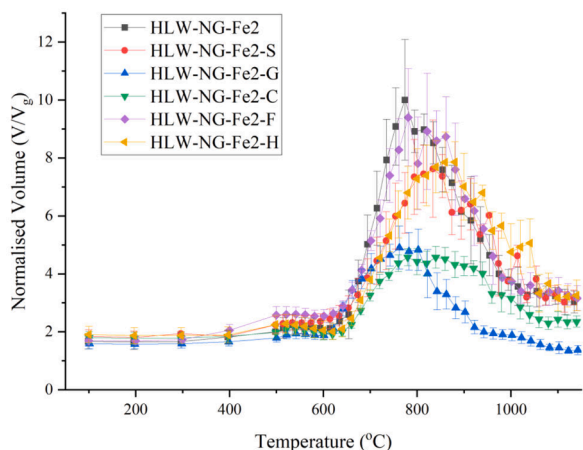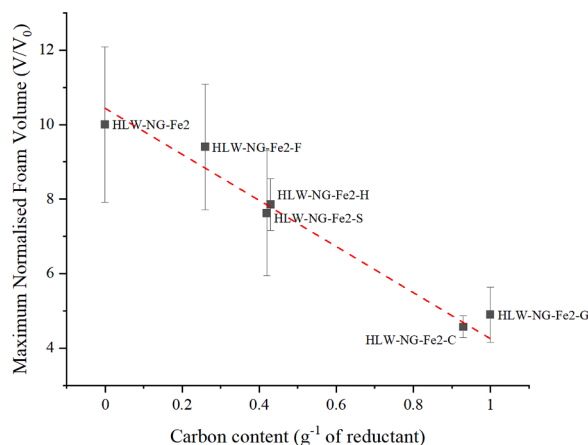The early gas evolution peaks, <200 ℃, given by TGA are likely

Fig. 2. Maximum normalised volume of pellets during Feed Expansion Test with carbon content per gram of reductant added.

Table 4
Foaming behaviour of feeds during melting from FETs and TGA.

Feed	C g^{-1} reductant	Normalised Maximum Foam Volume	Temperature of foam onset (℃)	Temperature of foam collapse* (℃)
HLW-NG-Fe2	–	10.0 ± 2.1	674 ± 10	774 ± 10
HLW-NG-Fe2-S	0.42	7.6 ± 1.7	674 ± 8	834 ± 9
HLW-NG-Fe2-G	1.0	4.9 ± 0.7	642 ± 2	762 ± 1
HLW-NG-Fe2-C	0.93	4.6 ± 0.3	680 ± 1	780 ± 1
HLW-NG-Fe2-F	0.26	9.4 ± 1.7	661 ± 2	781 ± 2
HLW-NG-Fe2-H	0.43	7.9 ± 0.7	680 ± 1	880 ± 1

* Foam collapse taken as $T_{FB} = T_{FM}$, temperature of foam collapse equal to temperature of foam maximum.

physical and chemical H_2O evolution which not captured by EGA in Fig. 4. The 200–600 ℃ range covers both chemical dehydration and most of the CO_2 evolution, Fig. 4. By EGA, most of the CO_2 evolution for all feeds occurs in a large peak centred around 500 ℃, which contributes only small mass loss events by TGA. The larger mass-loss peaks around 250 ℃ are therefore attributed to H_2O evolution. CO_2 evolution begins at lower temperatures for the HLW-NG-Fe2-S, -F and -H feeds, explaining some variance in the mass loss events in this temperature region by TGA, Fig. 3. The HLW-NG-Fe2-H feed has significant CO evolution in the 600–900 ℃ showing insufficient oxygen available to continue CO_2 evolution. CO_2 and CO evolution continue almost up to melt temperature at significant quantities in the HLW-NG-Fe2-G and C feeds. The evolution, or retention, of SO_2 is a consequence of the redox state of the melt and oxygen partial pressure [52].

Given the assumption made in Eqs. (2-6), that all C evolves as CO_2, we expect negative evolution of O_2 from the reductant added feeds. No O_2 is observed in EGA for these feeds, Fig. 4. Calculation of the maximum CO_2 evolved, under the assumption that all C in each

Fig. 1. Normalised volume of pellets during Feed Expansion Test with different reductant and raw material feeds.
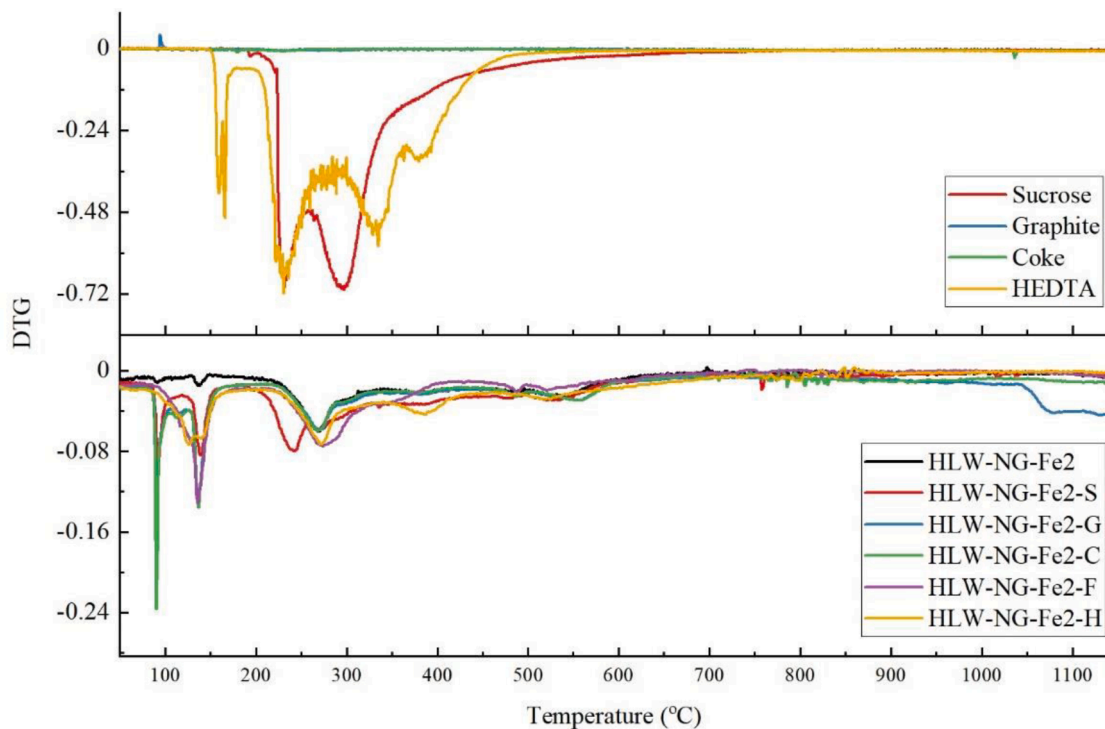
Fig. 3. Derivative of the thermogravimetric analysis (TGA) of some of the reductants (t) and feeds with added reductants (bottom) between room temperature and 1150 ℃.
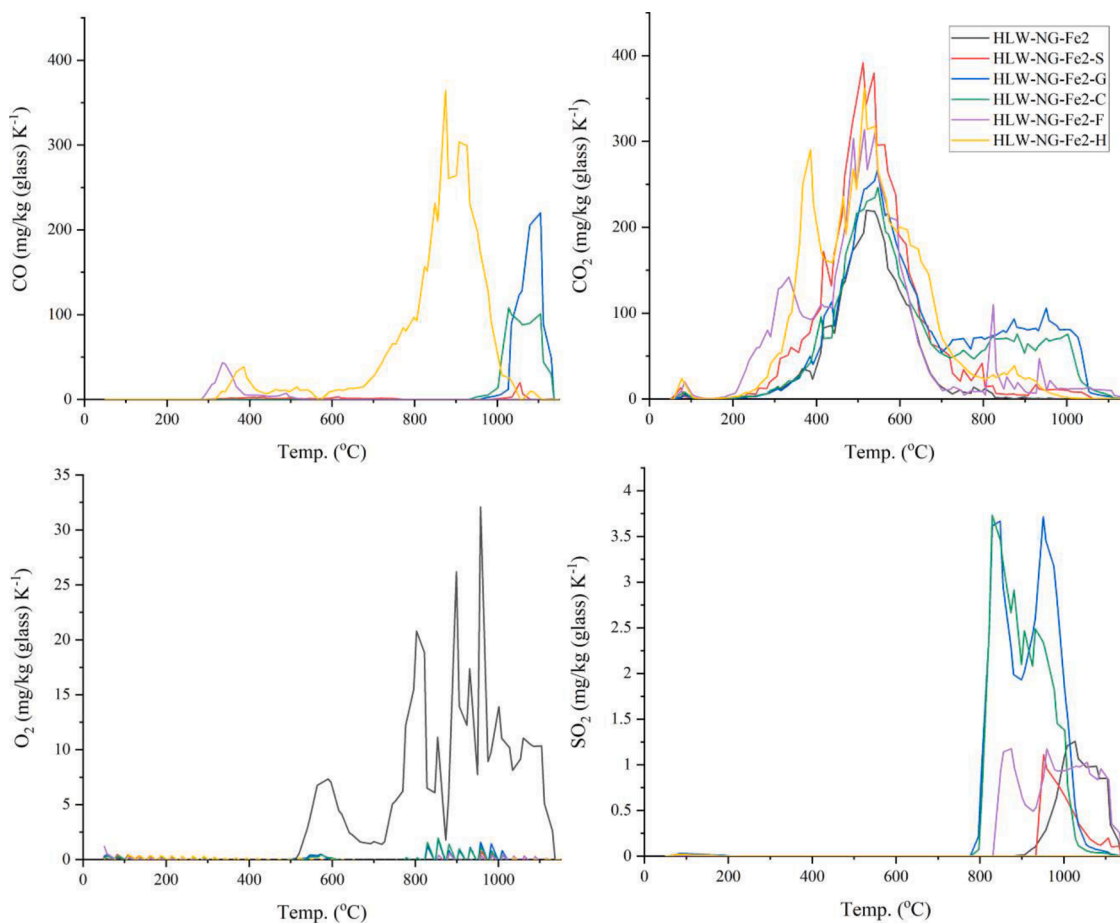

Fig. 4. Evolved CO (top left), CO_2 (top right), O_2 (bottom left) and SO_2 (bottom right) of all feeds during heating to 1150 ℃ in 50 ml min^{-1} He.

reductant evolves as CO_2, is given in Table 5 using the stoichiometry of the raw materials used during batching, compared with the final glass oxides, assuming all C evolved as CO_2, e.g. $Na_2CO_3 \rightarrow Na_2O + CO_2$. This is then compared with the evolved O_2, CO_2 and CO for each of the feeds measured by EGA, which highlights a negative O_2 balance, being the difference between the expected and measured, for all of the feeds.

Evolution of CO rather than CO_2, is a consequence of the negative O_2 balance, $C + \frac{1}{2} O_2 \rightarrow CO$ occurring rather than formation of CO_2, leads to a less negative oxygen balance. The final O_2 balance in Table 5, takes this calculation into account for evolved CO in each of the feeds. For the HLW-NG-Fe2 feed the quantity of C evolved as CO_2 is approximately as expected. For the HLW-NG-Fe2-S and -F there is a deficit in the total C evolved as either CO or CO_2 and the expected value added to the feed, this is even greater for the HLW-NG-Fe2-G and -C feeds. In these instances, it is possible that some C is retained in the final glass sample, unreacted. For -G and -C feeds this is supported by the analysis of decomposition of the reductants in Fig. 3. For the HLW-NG-Fe2-H feed, there is significantly more evolved CO and CO_2 than possible by the calculations of the amount of C added to the feed. All samples were created, and subject to EGA, under the same conditions, so the excess carbon remains unexplained, and potentially down to error in the data collection or air in-leakage in the system.

3.3. Phase evolution with temperature

Proportions of crystal phases forming during melting and the corresponding amorphous glass proportions, Fig. 5, were found by refining the XRD patterns to identified phases, comparing the intensities to the internal Si standard. The rate of dissolution of silica is similar amongst all of the feeds. The rate of Fe_2O_3 dissolution is slowest in the HLW-NG-Fe2 feed, all other feeds show less Fe_2O_3 at 800 and 1000 °C. By 1000 °C, no Fe_2O_3 remains in the HLW-NG-Fe2-C, -G and -H feeds. In HLW-NG-Fe2-S, there is some Fe_2O_3 remaining at 1150 °C. There is a spike in spinel phase in the HLW-NG-Fe2-C feed at 1000 °C.

For the Fe_3O_4-like spinel phases identified in each pattern the refined lattice parameters are given in Table 6. The refined lattice constants indicate potential deviation from stochiometric Fe_3O_4, $a = b = c$ of 8.394

Å [53], likely a mixture of Fe, Mn, Ni and Cr bearing spinels. Spinel structures with a mixture of Mn, Cr and Ni have been detected in previous studies of the HLW-NG-Fe2 simulated glass composition [10,17].

3.4. ^{57}Fe Mössbauer spectroscopy

^{57}Fe Mössbauer spectroscopy was performed on each of the samples to analyse the redox state and coordination of iron. The ^{57}Fe Mössbauer spectra for HLW-NG-Fe2, HLW-NG-Fe2-S and -F are shown in Fig. 6. Doublets with a centre shift, CS (mm s^{-1}), greater than 0.90, and quadrupole splitting, QS (mm s^{-1}), greater than 2.0 were attributed to Fe^{2+} phases [54]. Fitted parameters of the magnetic phases were compared to literature for identification [55–58]. The results of the Lorentzian fits of the spectra are tabulated in Appendix C.

All ^{57}Fe Mössbauer spectra shown in Fig. 6 contain paramagnetic doublets with centre shift (CS) and quadrupole splitting (QS) values corresponding to Fe^{3+}. At 600 °C and 800 °C only one paramagnetic phase is resolvable, however, there are consistently a minimum of 2 resolvable sites resolved at 1000 and 1150 °C. The two common sites between all three samples are tetrahedral paramagnetic Fe^{3+} sites with a CS between 0.25–0.27 mm s^{-1} and QS of 0.75–0.79 mm s^{-1} and 1.05–1.38 mm s^{-1}. The CS values of these sites are all within the range of tetrahedral Fe^{3+} [54] each sample has a site with relatively lower and higher QS, indicating a site where the electron cloud symmetry is distorted by local bonding, e.g. rather than Fe-O-Fe there are Fe-O-M bonds where M is an atom with a different electronegativity [59]. In the HLW-NG-Fe2-S sample at 1000 °C there is a $^{IV}Fe^{2+}$ phase contributing $2.4 \pm 2\%$ to the spectral area, which is only slightly above error. There is no Fe^{2+} phase detected in the 1150 °C sample.

Magnetically ordered dominant sextets at 600 and 800 °C belong to α-Fe_2O_3, with smaller contributions from Fe-bearing spinels with Fe^{3+} on the B site, and Fe, Mn or Ni likely on the A site [55]. The relative proportion of the spinel phases increases with decrease in the α-Fe_2O_3, in line with the phase ID by XRD in Section 3.3. At 1150 °C $24.8 \pm 2\%$ of the Fe in the HLW-NG-Fe2-S sample, and $14 \pm 2\%$ in the HLW-NG-Fe2-F sample, is in the α-Fe_2O_3 phase. There is a small amount of Fe_2O_3 detected in the HLW-NG-Fe2-S sample correlating with the XRD, Section 3.3.

^{57}Fe Mössbauer spectra for the HLW-NG-Fe2-G, -C and -H samples are grouped in Fig. 7. Fe^{2+} paramagnetic doublets emerge in all feeds with increasing heat treatment temperature. Samples quenched at 1150 °C show significant proportions of $^{VI}Fe^{2+}$, contributing 38.8 ± 2, 21.3 ± 2 and $11.8 \pm 2\%$ to the total spectral area for the HLW-NG-Fe2-G, -C and -H glasses, respectively. The reductants that had the greatest effect on foam reduction also had a reducing effect on the iron redox ratio in the paramagnetic phase, Fe^{3+}/Fe_T, in the final glass, as shown in Fig. 8.

The transition from α-Fe_2O_3 dominating the magnetically ordered components to Fe_3O_4-like spinels [55], occurs by 800 °C in the HLW-NG-Fe2-G and -H feeds, earlier than all of the other feeds, and 1000 °C in the HLW-NG-Fe2-C feed. This order is in agreement with the XRD in Section 3.3. All of the magnetic sextets in the 1150 °C samples are attributed to magnetite, Fe_3O_4, or a similarly structured spinel phase.

The redox ratios in the 1150 °C samples were determined by the proportion of Fe in each of the two paramagnetic phases, assuming that the recoil-free fraction ratio $f(Fe^{3+}/Fe^{2+}) = 1.0$. This assumption may overestimate the Fe^{3+}/Fe_T values [60]. The intermediate stages give indications of the temperatures at which the O_2 is evolved by these structural changes.

3.5. X-Ray absorption near edge spectroscopy

3.5.1. Mn K-edge

Mn K-edge spectra were calibrated using the absorption edge position of the measured standards, Mn-foil, MnO, Mn_2O_3 and MnO_2 [61, 62], applying the shift in eV to the sample data collected. Qualitatively,

Table 5

Expected and observed CO, CO_2 and O_2 evolution from calculations of gas balance.

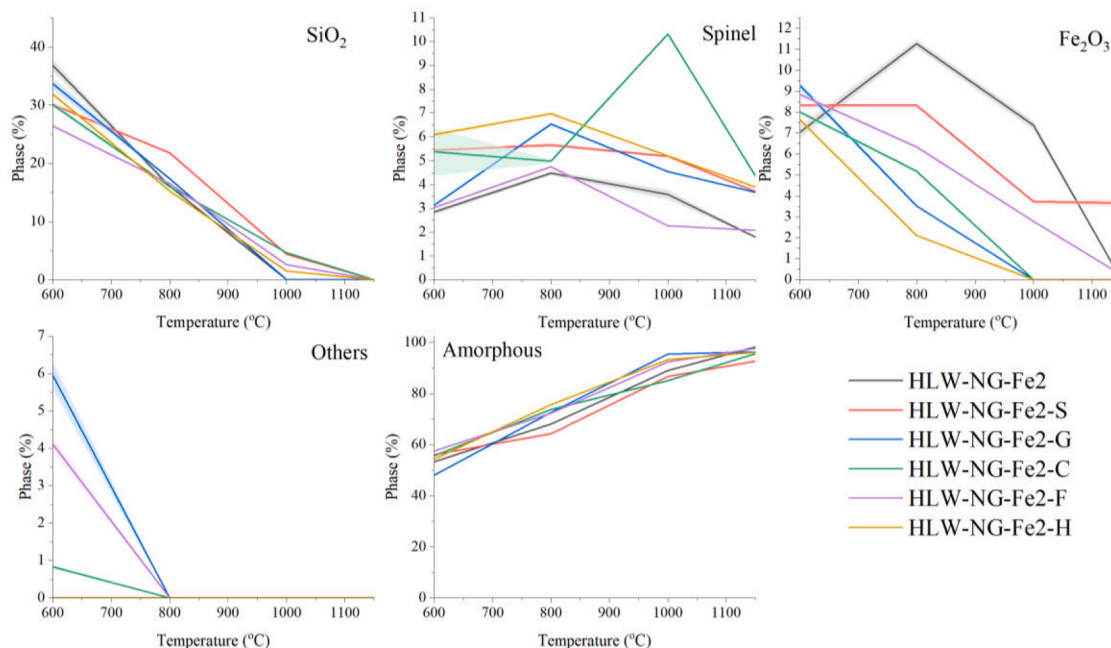| Feed	Calculated CO_2 mg kg^{-1} glass	Calculated O_2 mg kg^{-1} glass	CO_2 by EGA mg kg^{-1} glass	CO by EGA mg kg^{-1} glass	O_2 by EGA mg kg^{-1} glass	O_2 balance mg kg^{-1} glass
HLW-NG-Fe2	45,400	772	45,300	0	6600	−5828
HLW-NG-Fe2-S	106,000	−66,500	76,900	1000	0	−66,100
HLW-NG-Fe2-G	189,900	−104,600	75,600	22,400	0	−96,500
HLW-NG-Fe2-C	179,800	−94,500	67,900	15,400	0	−88,900
HLW-NG-Fe2-F	82,800	−28,500	72,400	2900	0	−27,400
HLW-NG-Fe2-H	107,500	−76,900	86,600	52,700	0	−57,700

Fig. 5. Evolution of phases with temperature by Rietveld refinement of X-ray diffraction Patterns.

Table 6
Refined lattice parameters for spinel phases identified in the final glasses.

Feed	Phase wt% in glass	Phase ID	ICDD Ref	Lattice Constants (Å)
HLW-NG-Fe2	1.7(04)	Fe_3O_4	01–076–1849	8.400(4)
HLW-NG-Fe2-S	3.52(2)	Fe_3O_4	01–088–0866	8.392(1)
HLW-NG-Fe2-G	3.49(2)	Fe_3O_4	04–009–4255	8.395(1)
HLW-NG-Fe2-C	4.15(3)	Fe_3O_4	00–019–0629	8.395(1)
HLW-NG-Fe2-F	1.98(2)	Fe_3O_4	04–008–4511	8.404(1)
HLW-NG-Fe2-H	3.70(3)	Fe_3O_4	01–087–2334	8.398(1)

the absorption edge in Mn spectra shifts linearly with oxidation state, and this method has been used to obtain an estimate of Mn oxidation state in previous studies [7,61,63,64]. All Mn K-edge spectra are given in Appendix D. The first inflection point of each of the Mn K-edge spectra was plotted against a linear fit of the first inflection point of each of the standards and their known oxidation states, Fig. 9 (left) [7,65]. This fit was used to approximate an average Mn oxidation state for the stages of melting samples, Fig. 9 (right).

Temperature had the effect of reducing Mn^{4+} in all of the feeds, particularly above 800 °C. For HLW-NG-Fe2-G, -C and -H the main reduction occurred between 800 and 1000 °C. The HLW-NG-Fe2-S and -F feeds, similarly to the HLW-NG-Fe2 feed, reduced most significantly between 1000 and 1150 °C.

3.5.2. Cr K-edge and Ce L_{iii} edge

Ce L_{III} and Cr K edges spectra were calibrated using measured standards, Cr_2O_3 and $Na_2Cr_2O_7$, for Cr [66–68] and CeO_2 and $Ce_2(C_2O_4)_3$ for Ce [69–71] and referenced literature values, applying the energy shift to each collected spectrum. All Cr K-edge and Ce L_{III}-edge spectra are given in Appendix E and F, respectively. A linear combination fitting (LCF) function was used to fit standard data [66–68] to each spectrum to determine the proportion of the element in each oxidation state, Fig. 10. Examples of LCF are given in Appendix G.

Some Cr oxidises from the Cr^{3+} raw material by 600 °C in the HLW-NG-Fe2 and HLW-NG-Fe2-S and -G feeds. Further oxidation in some feeds at 800 °C occurs, before reduction back to all Cr^{3+} by 1000 °C. Ce in all of the feeds reduces with temperature. As with Mn, they reduce in the order HLW-NG-Fe2-H, -G and -C, followed by -S by 1000 °C, and finally by HLW-NG-Fe2 and HLW-NG-Fe2-F at 1150 °C.

3.5.3. Summary of redox behaviour of multivalent species

The expected O_2 evolution due to the net change in redox from the feed to glass was calculated for each feed. Fig. 11 shows the expected O_2 evolution based on redox changes for each of the temperature stages measured, 600, 800, 1000 and 1150 °C, while Fig. 12 shows the total O_2 evolution by changes in redox throughout melting for each of the species measured. [57]Fe Mössbauer was used for iron redox, and XANES for chromium, manganese and cerium redox.

4. Discussion

4.1. Effects of reductants on foaming

The feed volume expansion results, Fig. 1, show the most effective additive for reduction of foam during melting. The order of reduction in maximum foam volume, was as follows,

Original < Formic Acid < HEDTA < Sucrose < Graphite < Coke

For HLW-NG-Fe2, HLW-NG-Fe2-S, -H, and -F, the order of maximum foam reduction correlates with the carbon content per gram of reductant added. Peak foam reduction with addition of carbon to the feed is expected [72]. At peak foam, coke was slightly more effective than graphite, however graphite had a greater effect on the foam reduction above peak foaming temperature. The mechanism of primary foam suppression is presently unclear. The primary foam peak is sensitive to both temperature and quantities of CO and CO_2 evolution, in the case of both coke and graphite additions, the EGA curves of these gases resembles the original HLW-NG-Fe2 feed. Both the viscosity of the melt, and particle size of reductant additions will influence also the kinetics of foaming and foam reduction [29,73,74], therefore further investigation of these reductants on the foam volume would be necessary for optimisation of the process.

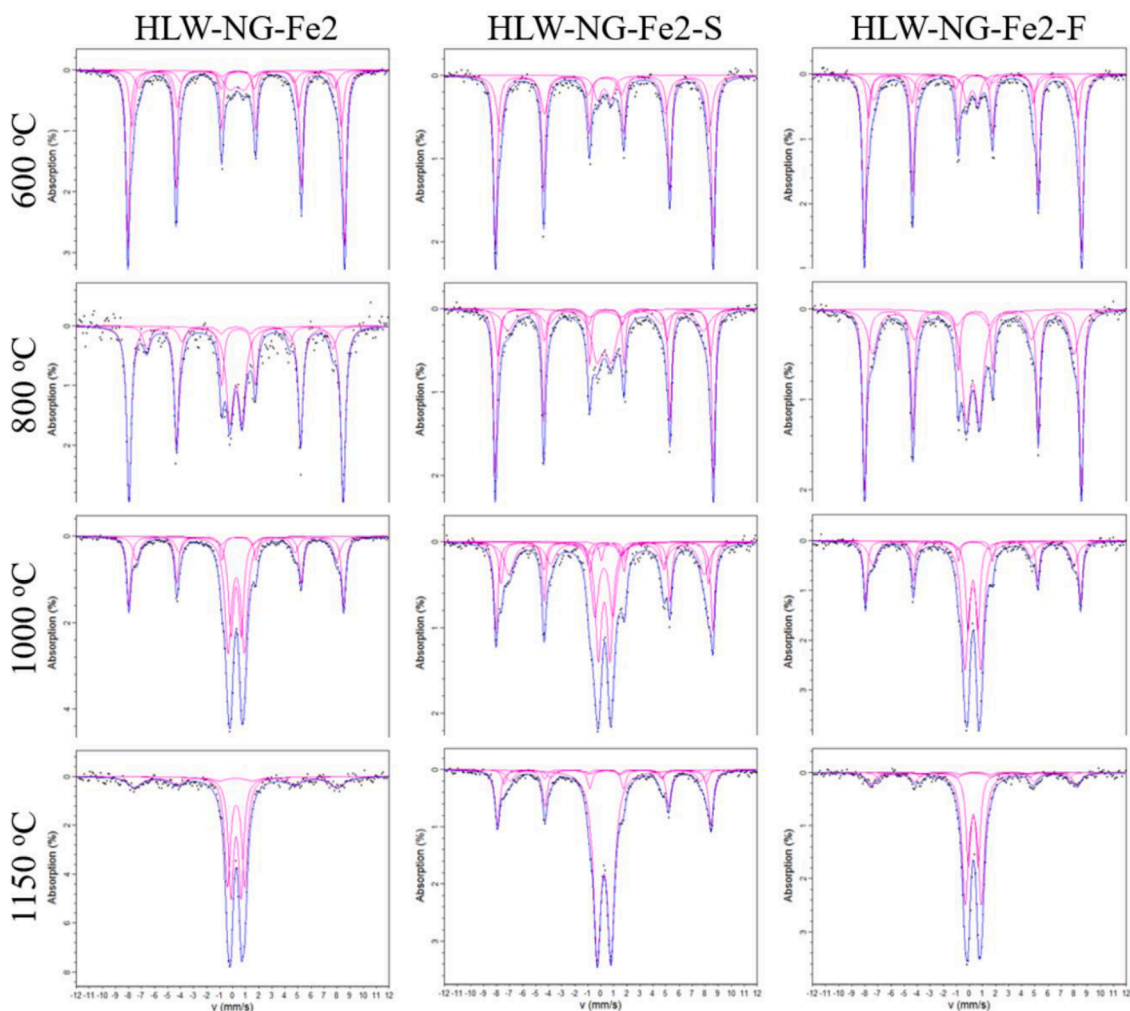Beyond the maximum primary foaming peak, there was considerable

Fig. 6. ^{57}Fe Mössbauer spectra for the HLW-NG-Fe2, HLW-NG-Fe2-S and -F feeds heated to 600, 800, 1000 and 1150 °C.

foaming up to melt temperature in the HLW-NG-Fe2, HLW-NG-Fe2-S, -F and -H feeds which was suppressed in the HLW-NG-Fe2-G and -C feeds to some extent. Both of these substances entirely supress O_2 evolution, however the other reductants also have this effect. The main contributions to this secondary foaming, based on EGA, are residual CO and CO_2 trapped in the melt and released in small quantities with increasing temperature along with smaller contributions from SO_2 and O_2. The continuous release of CO_2 above maximum foaming temperatures appears to correlate with reduced secondary foam.

4.2. Redox changes during melting

The iron redox state is often used as the measure of redox in a glass batch, and to quantify the oxygen partial pressure [18,75,76], which is a reasonable approximation for waste streams, or industrial glass batches and melts that contain high levels of iron, and insignificant amounts of other multivalent oxides. In work by Goldman [77], even when there is no detected ferrous iron in the glasses, there is oxygen evolution associated with other redox species such as chromium, cerium and manganese. Other multivalent species, Mn, Cr, Ni and Ce, have been investigated for a range of properties in commercial glass melting [78–82] and in radioactive waste streams [3,83,84].

4.2.1. Iron redox

For the feeds studied feeds, the rate of dissolution of Fe_2O_3 varied during melting. The slowest rate of dissolution of Fe_2O_3 is in the HLW-

NG-Fe2 feed, as predicted in the absence of additional reducing species [85]. The spinel structures are similar throughout the feeds, bearing most resemblance to magnetite, Fe_3O_4, $a = b = c = 8.394$, but are likely to also contain Mn, Cr and Ni, Table 5. Oxygen contributions of the spinel formation from haematite was considered negligible to the total balance of O_2 [12]. This evolution from Fe_2O_3 to Fe_3O_4-like spinel structure was also observed by ^{57}Fe Mössbauer spectroscopy Section 3.4.

By ^{57}Fe Mössbauer spectroscopy we observe a change in the redox state of iron in the paramagnetic phase in the HLW-NG-Fe2-S, -G, -C and -H samples. In the HLW-NG-Fe2-S sample the paramagnetic iron is reduced at 1000 °C and re-oxidises, in the -G, -C and -H samples there remains considerable Fe^{2+} in the final glasses. A reduction to a minimum of $Fe^{3+}/Fe_T = 0.5$ was observed previously in the HLW-NG-Fe2 feed at temperatures of 850–1150 °C by XANES [7], there is no apparent reduction in the Fe by ^{57}Fe Mössbauer spectrometry in the present study. While no studies have been found to report the iron redox ratio of Fe in glasses with coke additions, Ryan et al. [29] suggested that coke would have a greater affect than some reductants at higher temperatures, above the temperatures of glass-forming and foaming, and Kloužek et al. [52] reported an increase in refining efficiency in a commercial glass batch with coke addition of 0.02 wt% and a reducing effect on the glass.

Where the iron redox of feeds containing HEDTA has been measured previously, those feeds have also contained sucrose [31,86,87], therefore separating the effectiveness on reduction of multivalent species is not possible. In the present study 3 wt% HEDTA is shown to have a significant effect, reducing Fe^{3+}/Fe_T to 0.83. The low-temperature
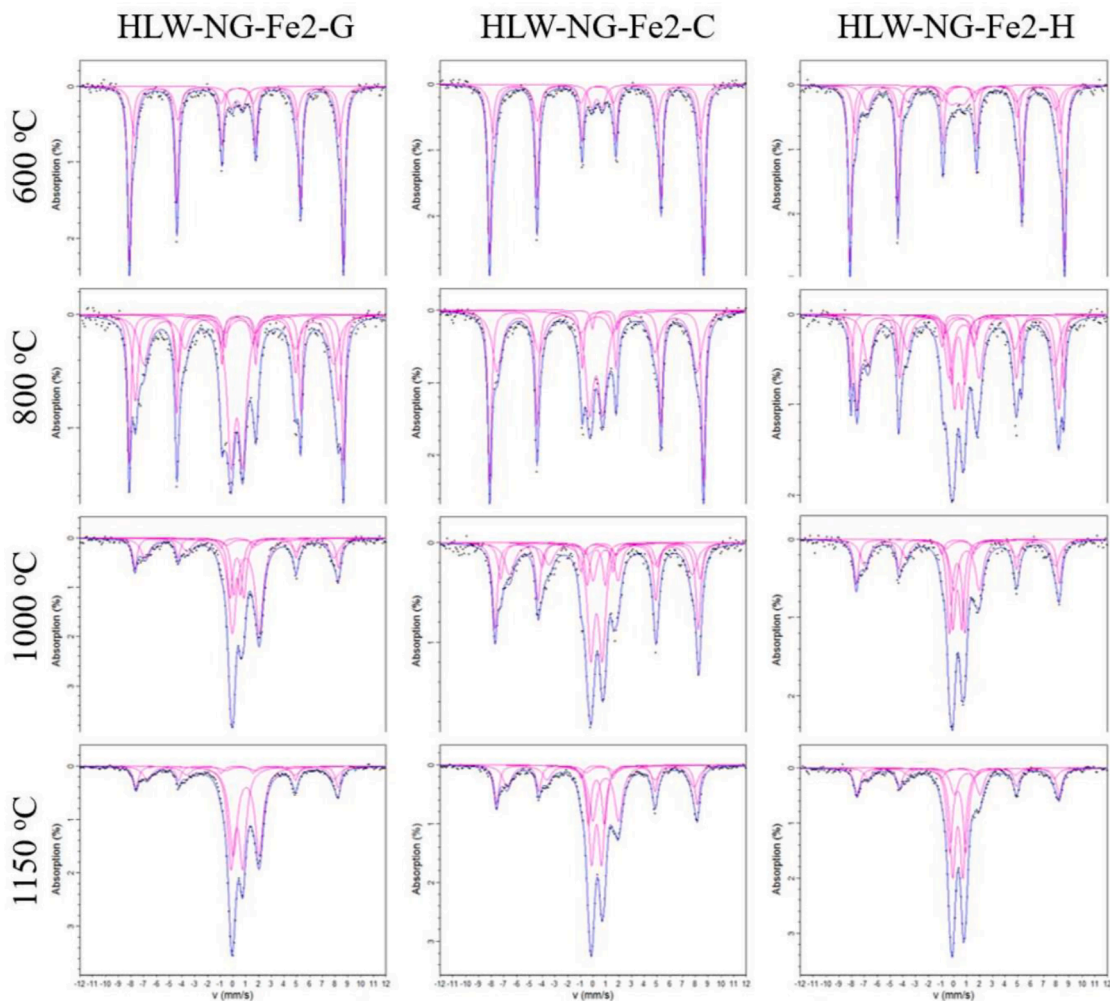
Fig. 7. ^{57}Fe Mössbauer spectra for the HLW-NG-Fe2-G, -C and -H feeds heated to 600, 800, 1000 and 1150 °C.
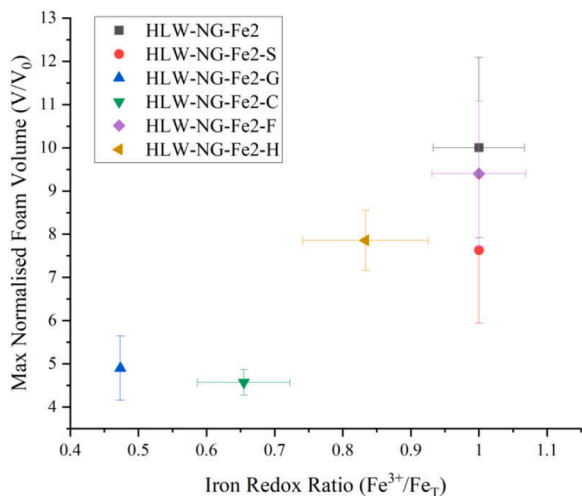

Fig. 8. Maximum normalised foam volume with estimated iron redox state by ^{57}Fe Mössbauer spectroscopy for the final glass samples.

decomposition of sucrose and formic acid, by the TGA observed in Fig. 3, would suggest that the early elimination of nitrates, or decomposition of the raw material [29,88] precludes any efficient high-temperature reduction of multivalent species [89]. However, previous studies have shown highly reduced glasses with varying sucrose additions [18,19,23] and ferrous iron content, up to $Fe^{3+}/Fe_T = 0$ [16] and 0.4 [90] for formic acid additions, to waste feed compositions.

From calculations of the O_2 contribution from a redox state change in Fe, by Eq. (7),

$$Fe_2O_3 \leftrightarrow 2FeO + \frac{1}{2} O_2, \qquad (7)$$

it has been determined that the HLW-NG-Fe2-G feed has the highest net O_2 contribution. HLW-NG-Fe2, HLW-NG-Fe2-S and -F feeds have no net change of redox state in the paramagnetic phase, and therefore no net O_2 contribution by this mechanism. These contributions to O_2 evolution begin to explain the highly negative O_2 balance for the reductant added feeds discussed in 3.2.

4.2.2. Manganese redox

In the present study, the manganese is approximately Mn^{4+} at 600 °C in the HLW-NG-Fe2 feed, consistent with the previous results for which the Mn^{4+} oxidation state was observed at 500 °C [7]. However, the same study of the feed quenched at 850 °C showed reduction to almost entirely Mn^{2+}, where the main reduction of Mn occurs between 1000 and 1150 °C in Fig. 9. Reduction of $Mn^{4+} \rightarrow Mn^{2+}$ follows, before any reduction of Ce^{4+}, at 800 °C, in the HLW-NG-Fe2, HLW-NG-Fe2-S and -H feeds. This is in agreement with the order predicted by the electromotive force series for the reduction potential of Mn^{3+}/Mn^{2+} [39,91]. The Mn^{4+} to Mn^{2+} continues all the way to Mn^{2+} in all feeds. Each of these reactions is preferential to the $Fe^{3+} \rightarrow Fe^{2+}$ reaction. Net contributions
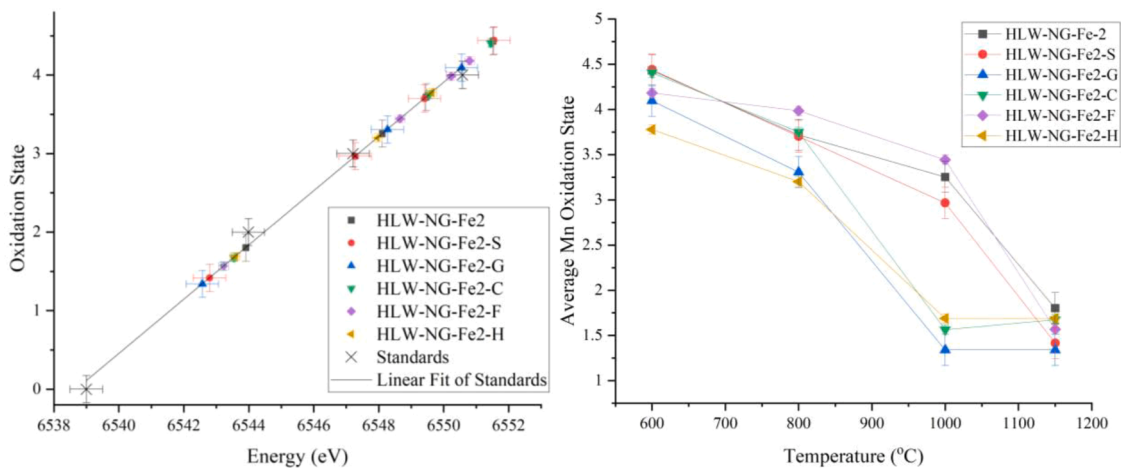
Fig. 9. Average Mn oxidation states determined by as a linear function of the standards (left) and associated oxidation states for each of the samples at 600, 800, 1000 and 1150 °C (right).
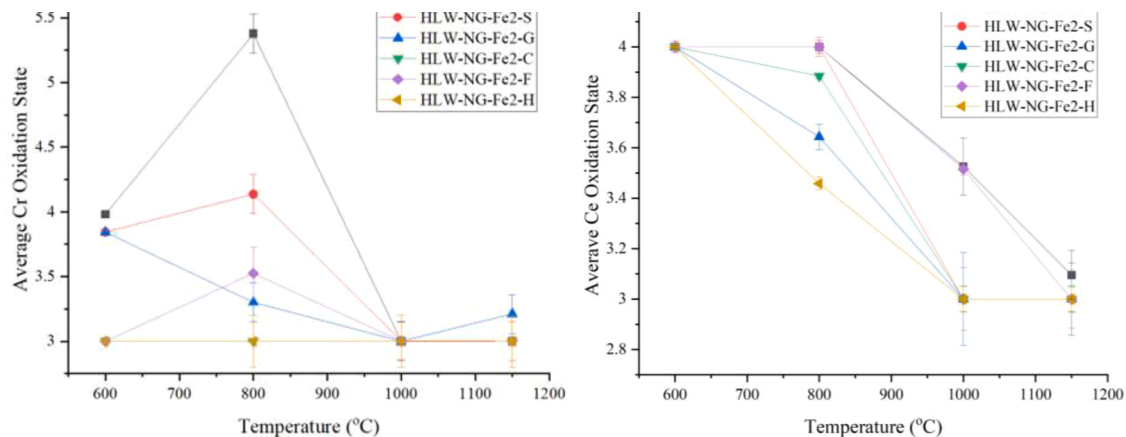

Fig. 10. Average Cr (left) and Ce (right) oxidation states determined by a LCF of the standards in different oxidation states for each of the samples at 600, 800, 1000 and 1150 °C.
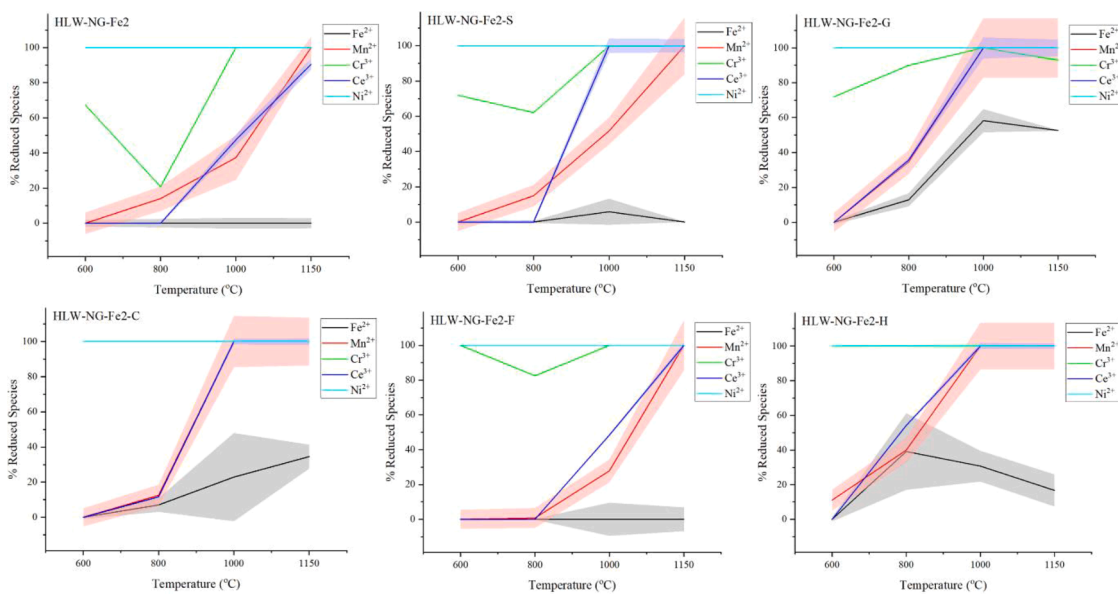

Fig. 11. Predicted evolved O_2 by redox reactions for each multivalent species in the feeds at 600, 800, 1000 and 1150 °C using XANES measurements for Mn, Cr and Ce and ^{57}Fe Mössbauer measurements for Fe.
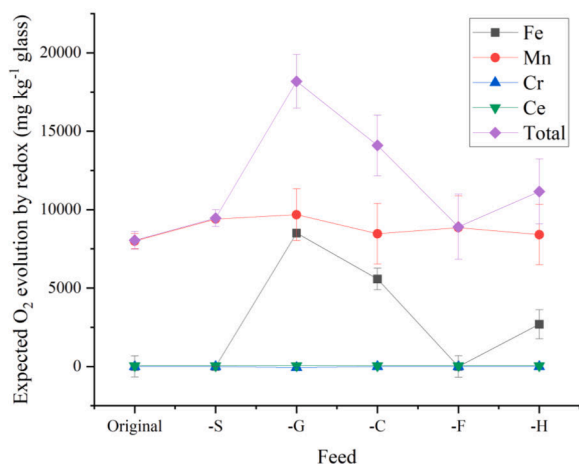
Fig. 12. Predicted net evolved O_2 by redox reactions for each multivalent species in the feeds using XANES measurements for Mn, Cr and Ce and ^{57}Fe Mössbauer measurements for Fe.

to O_2 evolution by reduction, or partial reduction of Mn^{4+} to Mn^{2+} were given by the following equation,

$$MnO_2 \leftrightarrow MnO + ½ O_2 \tag{8}$$

4.2.3. Chromium redox

As predicted by Schreiber's work, discussed in Section 1, reduction of any oxidised Cr^{6+} to Cr^{3+} preceded the reduction of the other species. The only deviation from this behaviour is observed in the HLW-NG-Fe2-G feed, where there is a re-oxidation of ~7% to Cr^{6+} at 1150 °C, which is only slightly above the limit of uncertainty. Previous collection of the Cr K-edge in the HLW-NG-Fe2 feed was not reported along with Mn and Fe K-edges as there was too much noise in the data [7]. However, the study did observe a similar trend in the HLW-E-M09 simulated waste feed, mostly Cr^{3+} was observed at 500 °C, and then a large increase occurred at 700 °C to over 80% Cr^{6+}, at higher temperatures, the Cr reduced again down to over 90% Cr^{3+} in the final glass [7].

For the HLW-NG-Fe2, HLW-NG-Fe2-S, -C, -H and -F feeds, since the oxidation state of Cr returns to the oxidation state of the raw material used during batching, there was no net contribution to O_2 evolution during melting, by the following equation,

$$2CrO_3 \leftrightarrow 3/2O_2 + Cr_2O_3 \tag{9}$$

For the HLW-NG-Fe2-G feed there is a net negative contribution due to the reoxidation of some Cr^{3+} to Cr^{6+}. At 1150 °C there is a small energetic barrier to overcome to oxidise Cr^{3+} to Cr^{6+} at −0.04, from the reduction potentials in Table 3. Oxidation may become energetically favourable for a short time, although Ce^{3+} would also be expected to oxidise to some Ce^{4+} preferentially, given the reduction potential of that reaction is −0.03. There is oxygen available in the melt and the atmosphere at these temperatures, evidenced by the continued evolution of CO, Fig. 4. It is stipulated here that with longer time at melt temperature the Cr^{6+} would reduce to entirely Cr^{3+} reaching equilibrium with the surrounding melt, although a longer dwell times would be needed to confirm this.

4.2.4. Cerium redox

Following the oxidation and reduction of Cr, the Ce^{4+} was most readily reduced to Ce^{3+} amongst all of the feeds. For all feeds, the proportion of reduced of Mn and Ce follows a very similar path with increasing temperature, particularly in the HLW-NG-Fe2-G and -C feeds. In the HLW-NG-Fe2 feed, the reduction to Ce^{3+} is incomplete by 1150 °C, where Mn^{4+} has fully reduced to Mn^{2+}. Based on the reduction

potentials and electromotive force series outlined in Section 1, we would expect the inverse to be true, completion of the Ce^{4+}/Ce^{3+} reaction prior to completion of Mn^{4+}/Mn^{2+} [36,91].

Ce was reduced significantly for HLW-NG-Fe2-G and -H feeds by 800 °C and further for all of the feeds by 1000 °C. Significant quantities of trivalent Ce^{3+} are often found in glasses made with CeO_2 because of its high reducibility [92–94], studies have shown that both increasing the melting temperature can increase the proportion of Ce^{3+} present in some glasses [81,93,94], as well as the choice of raw materials [93].

The contribution to O_2 evolution by a redox change in Ce is small given the relatively small amount of Ce oxide in the glass composition compared to Fe and Mn oxides, Table 1. The contribution was calculated using the following equation,

$$2CeO_2 \leftrightarrow Ce_2O_3 + ½ O_2 \tag{10}$$

4.3. Oxygen fugacity

The apparent oxygen fugacity the glass melt, -log(fO_2), can be inferred using the final redox states of the multivalent elements by Schreiber's equation, in Section 1, and comparisons to literature [36,39, 95]. A relationship was derived by Schreiber and colleagues for imposed oxygen fugacity in a borosilicate melt (SRL-131) from the DWPF and resulting redox states of key species. This provided a useful comparison for estimated oxygen partial pressure in the complex borosilicate glass melt in this study [95]. Estimated -log(fO_2) in the glasses is provided in Table 7, using the final estimated redox states of all multivalent species, predominantly Fe as it has the most control over oxygen fugacity [7].

These values, while estimations, are in agreement with other studies of glasses bearing similar amounts of Fe_2O_3 [3,15,18,41,79]. The effect of reductants on the dissolved oxygen in the borosilicate glass melt, has not been explicitly studied, however it is expected that carbonaceous materials will reduce the partial pressure of oxygen in glass melts [97–99]. The reductants which had the most negative oxygen balance in Table 5, namely graphite, coke and HEDTA, also had the most negative effect on the apparent oxygen fugacity.

Table 7
Estimated -log(fO_2) at 1150 °C by Fe^{3+}/Fe_T by ^{57}Fe Mössbauer spectroscopy, Cr K-edge, Ce L_{III}-edge and Mn K-edge XANES spectroscopy [95,96].

Glass	% Reduced Fe (^{57}Fe Mössbauer)	% Reduced Cr (XANES)	% Reduced Ce (XANES)	% Reduced Mn (XANES)	Estimated-log(fO_2) (log (kPa))
HLW-NG-Fe2	0 ± 7	100.0 ± 0.3	90.5 ± 3.2	100 ± 12	2
HLW-NG-Fe2-S	0 ± 0.1	100.0 ± 0.1	100.0 ± 3.8	100 ± 16	2
HLW-NG-Fe2-G	53 ± 0.2	92.9 ± 1.1	100.0 ± 4.8	100 ± 16	8
HLW-NG-Fe2-C	35 ± 7	100.0 ± 0.3	100.0 ± 1.8	100 ± 17	7
HLW-NG-Fe2-F	0 ± 7	100.0 ± 0.2	100.0 ± 1.6	100 ± 14	2
HLW-NG-Fe2-H	17 ± 9	100.0 ± 0.8	100.0 ± 1.7	100 ± 13	5–6

4.4. Balance of gases

In the present study, O_2 was available during melting in the electric furnaces used for the heat treatments, and the EGA was performed in a He atmosphere, limiting the interpretation of the gas balance. Table 8 provides an estimated balance of O_2 based on the data available. As calculated in Table 5, the total O_2 expected includes the stoichiometric evolution of O_2 from the batched raw materials should all C evolve as CO_2, minus the equivalent O_2 saved by the proportion of C evolving as CO_2.

The O_2 evolution from the formation of spinel crystals from haematite is assumed negligible at this stage, as it is likely insignificant at small quantities of spinel [12]. The theoretical O_2 evolution from net changes in the redox states of the multivalent species, Fig. 11, is given in Table 8, to provide a total expected O_2 evolution. The value of expected O_2 evolution is negative for all reductant added feeds, so it is unsurprising that little to no oxygen evolves, and the apparent oxygen fugacity is more negative for the HLW-NG-Fe2-G, -C and -H feeds. More reduced species would be expected based on the oxygen deficit for the HLW-NG-Fe2-H. Other explanations for the negative O_2 balance include consumption from the atmosphere, which is a consideration particularly necessary for this study where the heat treatments and EGA were performed in different atmospheres, and the potential for remaining unreacted reductants in the final glass samples. The latter is supported by the TGA of the reductants and gas balance in Table 5, particularly for the HLW-NG-Fe2-G and C feeds, however there is no evidence of remaining C in the glass samples was by XRD in Section 3.3 or by XRF of the final glasses given in the supplemental material section H.

Based on net redox change from raw material to final glasses, Fig. 12, Mn reduction, in theory, contributes significantly more to O_2 evolution for all feeds, apart from the -G and -C feeds where Fe was heavily reduced. Fe is often most abundant multivalent species, however, the other species such as Mn, where they are in significant quantities, should not be overlooked when considering contributions to foaming. While many estimations were made in the process of calculations due to the complexity of the system, the behaviour of the multivalent species was not well-predicted using the current models and previous work [7,12,15, 44]. For example, we would expect a larger reduction in Fe, given the lack of oxygen availability, which was not supported by ^{57}Fe Mössbauer spectroscopy. However, according to ^{57}Fe Mössbauer spectroscopy, all but HLW-NG-Fe2-G and C are within the upper limit for Fe^{2+} content in Hanford waste glasses, $Fe^{2+}/Fe_T < 0.33$ to prevent precipitation of metallic species [84,100].

5. Conclusions

Reductant additions to the HLW-NG-Fe2 feed at 3 wt% of graphite and coke (93% C) were most effective in reducing the maximum foam volume by $51 \pm 3\%$ in and $54 \pm 2\%$, respectively. Graphite reduced the total foam over the temperature range most significantly, showing no secondary foam behaviour. This high-temperature behaviour differentiates graphite as a reductant from those used previously. Graphite and coke both had the most reducing effect on the Fe redox state, while HEDTA also reduced the Fe considerably with little effect on the foam volume. A change of the baseline reductant used at the Hanford site from sucrose to graphite or coke, for feeds similar to the HLW-NG-Fe2, could provide considerable improvements to the melting rate. In terms of processability, precipitation of spinels with the addition of reductants would be a limiting factor. However, this study shows a very similar level of spinel precipitation in the final glasses for coke and the baseline, sucrose, while coke has a much greater effect on foam reduction. Further optimisation of particle size and varying amounts of the reductants would be required prior to adoption of these methods.

The redox states of the multivalent species Fe, Mn, Cr and Ce, reduced according to the reduction potentials of each species and the reducing atmosphere in the melt by the additions of carbon-based raw

Table 8

Expected and observed O_2 evolution based on calculations of gas balance and O_2 evolution from redox reactions, compared with observed O_2 evolution by EGA.

Sample	Expected O_2 evolution from all batch gasses[*] mg kg^{-1} glass	O_2 from Redox[**] mg kg^{-1} glass	Total Expected O_2 Evolution mg kg^{-1} glass	O_2 evolved by EGA mg kg^{-1} glass
HLW-NG-Fe2	800	8000 ± 900	8800 ± 900	6600
HLW-NG-Fe2-S	−66,100	9500 ± 400	$-56,600 \pm 400$	0
HLW-NG-Fe2-G	−96,500	$18,200 \pm 500$	$-78,300 \pm 500$	0
HLW-NG-Fe2-C	−88,900	$14,100 \pm 700$	$-74,800 \pm 700$	0
HLW-NG-Fe2-F	−27,400	8900 ± 700	$-18,500 \pm 700$	0
HLW-NG-Fe2-H	−57,700	$11,200 \pm 900$	$-46,500 \pm 900$	0

[*] including $CO_2 \rightarrow CO + \frac{1}{2} O_2$.
[**] with XANES for Cr, Mn and Ce and ^{57}Fe Mössbauer for Fe.

materials. The overall contributions to O_2 evolution of each of the redox changes was devised as well as the total O_2 evolution from the feed raw materials, giving a negative O_2 balance for all reductant-added feeds, and leading to no O_2 evolution by EGA. The analysis techniques used for these calculations were performed in different atmospheres, therefore interpretation of the oxygen balance is qualitative. Evaluation of the redox states of multivalent species, and the inferred melt oxygen fugacity in the complex borosilicate glass with additions of a variety of reductant sources has not been studied previously. The calculations made of the O_2 balance, in particular, do not predict the reduction behaviour of the multivalent species in the melt. The general order of reducing species is predicted based on their reduction potentials, $Mn^{3+}/Mn^{2+} > Cr^{6+}/Cr^{3+} > Ce^{3+}/Ce^{4+} > Fe^{3+}/Fe^{2+}$, however the final oxidation states, given the calculations of O_2 balance are not well predicted using the simple electromagnetic force series outlined in the introduction, with a variance of 7% in the expected reduction of Cr^{6+}/Cr^{3+}. Further models have been developed since, to particularly address redox reactions within the cold cap for US waste treatment programs (Hanford and Savannah River sites) [84]. The results of this work aim to provide further data to improve these model predictions for wastes high in multivalent species.

Data availability

Data will be made available on request.

Acknowledgements

Supplementary materials

Supplementary material associated with this article can be found, in the online version, at doi:10.1016/j.jnoncrysol.2023.122240.

References

[1] K. Xu, P. Hrma, J.A. Rice, M.J. Schweiger, B.J. Riley, N.R. Overman, A.A. Kruger, Conversion of Nuclear Waste to Molten Glass: cold-Cap Reactions in Crucible Tests, J. Am. Ceram. Soc. 99 (2016) 2964–2970.

[2] R. Pokorný, P.R Hrma, Model for the conversion of nuclear waste melter feed to glass, J. Nucl. Mater. 445 (2014) 190–199.

[3] C.M. Jantzen, M.E. Stone, Role of Manganese Reduction/Oxidation (REDOX) On Foaming and Melt Rate in High Level Waste (HLW) Melters (U), Savannah River National Laboratory, Aiken, SC, US, 2007. WSRC-STI-2006-00066.

[4] R.Hilliard Pokorný, Z.J. Dixon, D.R. Schweiger, M.J. Post Guillen, D. Kruger, A. A. Hrma P, One-dimensional cold cap model for melters with bubblers, J. Am. Ceram. Soc. 98 (2015) 3112–3118.

[5] P.R Hrma, M.J. Schweiger, C.J. Humrickhouse, J.A. Moody, R.M. Tate, T. T. Rainsdon, N.E. Tegrotenhuis, Effect of glass-batch makeup on the melting process, Ceram. - Silikaty 54 (2010) 193–211.

[6] S. Lee, W.C. Eaton, P. Hrma, A.A. Kruger, Glass production rate in electric furnaces for radioactive waste vitrification, J. Am. Ceram. Soc. 102 (2019).

[7] D.P. Guillen, S. Lee, P. Hrma, J. Traverso, R. Pokorný, J. Klouẑek, A.A. Kruger, Evolution of chromium, manganese and iron oxidation state during conversion of nuclear waste melter feed to molten glass, J. Non Cryst. Solids 531 (2020), 119860.

[8] S.H. Henager, P. Hrma, K.J. Swearingen, M.J. Schweiger, J. Marcial, N. E. TeGrotenhuis, Conversion of batch to molten glass, I: volume expansion, J. Non Cryst. Solids 357 (2011) 829–835.

[9] R.G.C. Beerkens, J Van Der Schaaf, Gas release and foam formation during melting and fining of glass, J. Am. Ceram. Soc. 89 (2006) 24–35.

[10] K.S. Matlack, I.L. Pegg, I. Joseph, W.K. Kot, Support For HLW Direct Feed - Phase 2, Catholic University of America, DC, (United States), 2015. VSL-15R3440-1.

[11] Matlack, K.S. Gan, H. Chaudhuri, M. Kot, W.K. Pegg, I.L. Joseph, I. Kruger A.A. Melter throughput enhancements for high-iron HLW office of river protection, WA. (United States) ORP-54002. (2012).

[12] S.Hrma Lee, P. Klouẑek, J. Pokorný, R. Hujová, M. Dixon, D.R. Schweiger, M. J. Kruger, A. A. Balance of oxygen throughout the conversion of a high-level waste melter feed to glass, Ceram. Int. 43 (2017) 13113–13118.

[13] P. Hrma, Melting of foaming batches: nuclear waste glass, in: Advances in Fusion and Processing of Glass. in Conference on Advances in Fusion and Processing of Glass Dusseldorf (Germany, F. R.), 1990, 22-25 Oct 1990.

[14] D.R.Schweiger Dixon, M.J. Riley, B.J. Pokorný, R, P Hrma, Temperature distribution within a cold cap during nuclear waste vitrification, Environ. Sci. Technol. 49 (2015) 8856–8863.

[15] O. Pinet, I. Hugon, S Mure, Redox control of nuclear glass, Procedia Mater. Sci. 7 (2014) 124–130.

[16] D.F. Bickford, R.B. Diemer Jr, Redox control of electric melters with complex feed compositions, J. Non-Crystalline Solids1 84 (1986) 276–284.

[17] K.S. Matlack, C. Viragh, W.K. Kot, I.L. Pegg, I. Joseph, Effect of the Form of Iron on HLW Melt Rate, Catholic University of America, DC, (United States), 2015. VSL-15R3430-1.

[18] M.Pokorný Hujová, R. Klouẑek, J. Lee, S. Traverso, J.J. Schweiger, M.J. Kruger, a. A. Hrma P, Foaming during nuclear waste melter feeds conversion to glass: application of evolved gas analysis, Int. J. Appl. Glass Sci. 9 (2018) 487–498.

[19] C.J.Klouẑek Appel, J. Jani, N. Lee, S. Dixon, D.R. Hrma, P. Pokorný R, A. A. Kruger, M.J. Schweiger, Effect of sucrose on foaming and melting behavior of a low-activity waste melter feed, J. Am. Ceram. Soc. 102 (2019) 7594–7605.

[20] Carl, D.E. Paul, J. Foran, J.M. & Brooks, R. West valley demonstration project vitrification process equipment functional and checkout testing of systems (FACTS). West valley demonstration project, West Valley, NY (United States). DOE/NE/44139-64 (1990).

[21] R.G. Seymour, Evaluation of Alternative Chemical Additives for High-Level Waste Vitrification Feed Preparation Processing, Westinghouse Hanford Co., Richland, WA (United States), 1995. WHC-SD-WM-SP-009.

[22] P.A. Smith, J.D. Vienna, P Hrma, The effects of melting reactions on laboratory-scale waste vitrification, J. Mater. Res. 10 (1995) 2137–2149.

[23] I.S.Viragh Muller, C. Gan, H. Matlack, S. K, I.L Pegg, Iron Mössbauer redox and relation to technetium retention during vitrification, Hyperfine Interact. 191 (2009) 17–24.

[24] Kruger, A.A., Matlack, K.S., Pegg, I.L., Kot, W.K. & Joseph, I. Redox control for hanford HLW Feeds. Richland, WA (United States), VSL-12R2530-12 (2012).

[25] M. Arkosiová, J. Klouẑek, L. Nìmec, The role of sulfur in glass melting processes, Ceram. - Silikaty 52 (2008) 155–159.

[26] M. Vernerová, J. Klouẑek, L. Nĕmec, Reaction of soda-lime-silica glass melt with water vapour at melting temperatures, J. Non Cryst. Solids 416 (2015) 21–30.

[27] A.G. Fedorov, L. Pilon, Glass foams: formation, transport properties, and heat, mass, and radiation transfer, J. Non Cryst. Solids 311 (2002) 154–173.

[28] Matyáš, J. & Hrma, P. Sulfate fining chemistry in oxidized and reduced soda-lime-silica glasses (G Plus Project for Visteon Inc.). Richland, WA, (United States) PNNL - 15175 (2005).

[29] J.L. Ryan, Redox Reactions and Foaming in Nuclear Waste Glass Melting, Pacific Northwest National Laboratory, Richland, WA (United States), 1995. PNL-10510.

[30] A.A. Kruger, K.A. Matlack, I.L. Pegg, W. Gong, Final Report - Glass Formulation Testing to Increase Sulfate Volatilization from Melter, Catholic University of America, DC, (United States), 2013. VSL-04R4970-1, Rev. 0.

[31] K.S. Matlack, I.L. Pegg, W. Gong, Final Report: Compositional Variation Tests on DuraMelter 100 With LAW Sub-Envelope A3 Feed in Support of the LAW Pilot Melter, Catholic University of America, DC, (United States), 2003. VSL-01R62N0-1, Rev. 2.

[32] Kelly, S.E. A Joule-heated melter technology for the treatment and immobilization of low-activity waste. Washington river protection solutions report. Hanford Site (HNF), Richland, WA (United States). RPP-48935 (2011).

[33] S.F. Agnew, J. Boyer, R. Corbin, T.B. Duran, K.A. Jurgenson, J.R. FitzPatrick, T. P. Ortiz, B.L. Young, Hanford Tank Chemical and Radionuclide Inventories: HDW Model Rev. 4, Los Alamos National Laboratory, NM (United States), 1997. LA-UR-96-3860.

[34] H.D. Schreiber, Redox processes in glass-forming melts, J. Non Cryst. Solids 84 (1986) 129–141.

[35] H.D. Schreiber, R.C. Merkel Jr., V.L. Schreiber, G.B Balazs, Mutual interactions of redox couples via electron exchange in silicate melts: models for geochemical melt systems, J. Geophys. Res. 92 (1987) 9233–9245.

[36] H.D. Schreiber, N.R. Wilk, C.W. Schreiber, Comprehensive electromotive force series of redox couples in soda-lime-silicate glass, J. Non Cryst. Solids 253 (1999) 68–75.

[37] J. Marcial, J. Klouẑek, M. Vernerová, P. Ferkl, S. Lee, D. Cutforth, P. Hrma, A. A. Kruger, R. Pokorný, Effect of Al and Fe sources on conversion of high-level nuclear waste feed to glass, J. Nucl. Mater. 559 (2021).

[38] S.M.Ferkl Lee, P. Pokorný, R. Klouẑek, J. Hrma, P. Eaton, W.C. Kruger, A. A, Simplified melting rate correlation for radioactive waste vitrification in electric furnaces, J. Am. Ceram. Soc. 103 (2020) 5573–5578.

[39] H.D. Schreiber, G.B. Balazs, An electromotive force series for redox couples in a borosilicate melt: the basis for electron exchange interactions of the redox couples, J. Non Cryst. Solids 71 (1985) 59–67.

[40] B. Mirhadi, B Mehdikhani, Effect of manganese oxide on redox iron in sodium silicate glasses, Adv. Mater. 13 (2011) 1309–1312.

[41] W. Thiemsorn, K. Keowkamnerd, S. Phanichphant, P. Suwannathada, H Hessenkemper, Influence of glass basicity on redox interactions of iron-manganese-copper ion pairs in soda-lime-silica glass, Glas. Phys. Chem. 34 (2008) 19–29.

[42] H.D.Balazs Schreiber, G.B. Carpenter, B.E. Kirkley, J.E. Minnix, L.M. Jamison, L. P, T.O Mason, An electromotive force series in a borosilicate glass-forming melt, J. Am. Ceram. Soc. 67 (1984). C-106-C-108.

[43] R. Brückner, Redox ratio shifts and electrical transport properties in redox pairs containing glasses, J. Non-Crystalline Solids1 71 (1985) 49–57.

[44] O. Pinet, R. Guirat, J. Phalippou, T. Advocat, Development of models to predict the redox state of nuclear waste containment glass. in Nuclear fuel cycle for a sustainable future, Atalante, France (2008).

[45] A. Matthai, O. Claußen, D. Ehrt, C. Rüssel, Thermodynamics of redox equilibria and diffusion of polyvalent ions, Glas. Ber. Glas. Sei. Tec 71 (1998).

[46] S.D. Gates-Rector, T.N. Blanton, The powder diffraction file: a quality materials characterisation database, Powder Diffr. 34 (2019) 352–360.

[47] T. Degen, M. Sadki, E. Bron, U. König, G. Nénert, The high score suite, Powder Diffr. 29 (2014) S13–S18.

[48] H.M. Rietveld, A profile refinement method for nuclear and magnetic structures, J. Appl. Crystallogr. 2 (1969) 65–71.

[49] S.D. Brown, L. Bouchenoire, D. Bowyer, J. Kervin, D. Laundy, M.J. Longfield, D. Mannix, D.F. Paul, A. Stunault, P. Thompson, M.J. Cooper, C.A. Lucas, W. G. Stirling, The XMaS beamline at ESRF: instrumental developments and high resolution diffraction studies, J. Synchrotron Radiat. 8 (2001) 1172–1181.

[50] A.J. Dent, G. Cibin, S. Ramos, A.D. Smith, S.M. Scott, L. Varandas, M.R. Pearson, N.A. Krumpa, C.P. Jones, P.E. Robbins, B18: a core XAS spectroscopy beamline for Diamond, J. Phys. Conf. Ser. 190 (2009).

[51] B. Ravel, M. Newville, ATHENA and ARTEMIS: interactive graphical data analysis using IFEFFIT, Phys. Scr., T T115 (2005) 1007–1010.

[52] J. Klouẑek, M. Arkosiová, L. Nĕmec, Redox equilibria of sulphur in glass melts, Ceram. - Silikaty 50 (2006) 134–139.

[53] M.G. Brik, A. Suchocki, A. Kamińska, Lattice parameters and stability of the spinel compounds in relation to the ionic radii and electronegativities of constituting chemical elements, Inorg. Chem. 53 (2014) 5088–5099.

[54] M. Darby Dyar, A review of Mössbauer data on inorganic glasses: the effects of composition on iron valency and coordination, Am. Mineral. 70 (1985) 304–316.

[55] S.J. Oh, D.C. Cook, H.E Townsend, Characterisation of iron oxides commonly formed as corrosion products on steel, Hyperfine Interact. 112 (1998) 59–65.

[56] R.V.Klingelhöfer Morris, G. Schröder, C. Rodionov, D.S. Yen, Albert S. Ming, D. W. de Souza, A. Wdowiak Jr, T. Fleischer, I. Gellert, R. Bernhardt, B. Bonnes, U. Cohen, B.A. Evlanov, E.N. Foh, J. Gütlich, P. Kankeleit, E. McCoy, T. Mittlefehldt, D.W. Renz, F. Schmidt, M.E. Zubkov, B. Squyres, W. Steven, R. E Arvidson, Mössbauer mineralogy of rock, soil, and dust at Meridiani Planum, Mars: opportunity's journey across sulfate-rich outcrop, basaltic sand and dust, and hematite lag deposits, J. Geophys. Res. 111 (2006).

[57] I. Dézsi, I. Szucs, E. Sváb, Mossbauer spectroscopy of spinels, J. Radioanal. Nucl. Chem. 246 (2000) 15–19.

[58] A.A. Maksimova, A.V. Chukin, I. Felner, M.I. Oshtrakh, Spinels in meteorites: observation using Mössbauer spectroscopy, Minerals 9 (2019).

[59] J.G.Travis Stevens, C, J, J.R. DeVoe, Mössbauer Spectrometry, Anal. Chem. 44 (5) (1972) 384–406.

[60] H.L. Zhang, E. Cottrell, P.A. Solheid, K.A. Kelley, M.M. Hirschmann, Determination of $Fe^{3+}/\Sigma Fe$ of XANES basaltic glass standards by Mössbauer spectroscopy and its application to the oxidation state of iron in MORB, Chem. Geol. 479 (2018) 166–175.

[61] D.A. McKeown, W.K. Kot, H. Gan, I.L. Pegg, X-ray absorption studies of manganese valence and local environment in borosilicate waste glasses, J. Non Cryst. Solids 328 (2003) 71–89.

[62] M. Belli, A. Scafati, A. Bianconi, S. Mobilio, L. Palladino, A. Reale, E. Burattini, X-ray absorption near edge structures (XANES) in simple and complex Mn compounds, Solid State Commun. 35 (1980) 355–361.

[63] M. Abuín, A. Serrano, J. Chaboy, M.A. García, N. Carmona, XAS study of Mn, Fe and Cu as indicators of historical glass decay, J. Anal. At. Spectrom. 28 (2013) 1118–1124.

[64] A.C.Stanjek Scheinost, H. Schulze, D.G. Gasser, U, D.L Sparks, Structural environment and oxidation state of Mn in goethic-groutite solid-solutions, Am. Mineral. 86 (2001) 139–146.

[65] S.J.A. Figueroa, F.G. Requejo, E.J. Lede, L. Lamaita, M.A. Peluso, J.E. Sambeth, XANES study of electronic and structural nature of Mn-sites in manganese oxides with catalytic properties, Catal. Today 107–108 (2005) 849–855.

[66] A.J. Davenport, A.J. Aldykiewicz Jr., H.S. Isaacs, M.W. Kendig, A.M Mundy, XANES Studies of Chromate Replacements in Oxide Films On Aluminum, Brookhaven National Lab., Upton, NY (United States), 1991.

[67] S.G. Eeckhout, N. Bolfan-Casanova, C. McCammon, S. Klemme, E. Amiguet, XANES study of the oxidation state of Cr in lower mantle phases: periclase and magnesium silicate perovskite, Am. Mineral. 92 (2007) 966–972.

[68] Calmano, C., Mangold, S. & Welter, E. Speciation of Chromium compounds in contaminated soil samples by XANES. Energy 20, 6–7.

[69] J. Ueda, M. Katayama, K. Asami, J. Xu, Y. Inada, S. Tanabe, Evidence of valence state change of Ce^{3+} and Cr^{3+} during UV charging process in $Y_3Al_2Ga_3O_{12}$ persistent phosphors, Opt. Mater. Express 7 (2017) 2471.

[70] Q.G.Hua Ren, Y. Shen, H. Zhong, L. Jin, C.Z. Mi, Y. Yao, H.Y. Xie, Y.N. Wei, Q. S, L.W Zhou, Cytochemical behavior of rare earth ions in Euglena gracilis studied by XAFS, J. Radioanal. Nucl. Chem. 272 (2007) 359–362.

[71] Y. Takahashi, H. Sakami, M. Nomura, Determination of the oxidation state of cerium in rocks by Ce L_{III}-edge X-ray absorption near-edge structure spectroscopy, Anal. Chim. Acta 468 (2002) 345–354.

[72] J.C.Dixon Rigby, D.R. Cutforth, D.A. Marcial, J. Kloužek, J. Pokorný, R. Kruger, A.A. Scrimshire, A. Bell, M.T. A, P.A Bingham, Melting behaviour of simulated radioactive waste as functions of different redox iron-bearing raw materials, J. Nucl. Mater. 569 (2022) 153946.

[73] M. Liukkonen, K. Penttilä, P. Koukkari, A Compilation of Slag Foaming Phenomenon research: Theoretical studies, Industrial Experiments and Modelling, VTT Technical Research Centre of Finland, Tampere, Finland, 2012.

[74] D. Yu, M. Zhu, T.A. Utigard, M. Barati, TG/DTA study on the carbon monoxide and graphite thermal reduction of a high-grade iron nickel oxide residue with the presence of siliceous gangue, Thermochim. Acta 575 (2014) 1–11.

[75] N.F. Zhernovaya, V.I. Onishchuk, B. Davydoglu, Color control and redox balance monitoring in container glass, Glas. Ceram. (English Transl. Steklo i Keramika) 64 (2007) 111–114.

[76] D.F. Bickford, A. Applewhite-Ramsey, C.M. Jantzen, K.G Brown, Control of radioactive waste glass melters: i, preliminary general limits at Savannah river, J. Am. Ceram. Soc. (1990) 2896–2902.

[77] D.S. Goldman, Melt foaming, foam stability and redox in nuclear waste vitrification, J. Non Cryst. Solids 84 (1986) 292–298.

[78] M. Hubert, A.J. Faber, F. Akmaz, H. Sesigur, E. Alejandro, T. Maehara, S.R. Kahl, Stabilization of divalent chromium Cr (II) in soda – lime – silicate glasses, J. Non Cryst. Solids 403 (2014) 23–29.

[79] M. Hubert, A.J. Faber, H. Sesigur, F. Akmaz, S.R. Kahl, E. Alejandro, T. Maehara, Impact of redox in industrial glass melting and importance of redox control, in: Proceedings of the 75th Conference on Glass Problems, (S. K. Sundaram), 2017, pp. 113–128.

[80] P.A. Bingham, C.M. Jackson, Roman blue-green bottle glass: chemical-optical analysis and high temperature viscosity modelling, J. Archaeol. Sci. 35 (2008) 302–309.

[81] A. Wondergem-de Best, Redox Behaviour and Fining of Molten Glass, Eindhoven University of Technology, Eindhoven, The Netherlands, 1994. Ph. D. Thesis.

[82] O. Villain, G. Calas, L. Galoisy, L. Cormier, XANES determination of chromium oxidation states in glasses: comparison with optical absorption spectroscopy, J. Am. Ceram. Soc. 90 (2007) 1–23.

[83] P. Hrma, J.D. Vienna, B.K. Wilson, T. Plaisted, S.M. Heald, Chromium phase behavior in a multi-component borosilicate glass melt, J. Non Cryst. Solids 352 (2006) 2114–2122.

[84] C.M. Jantzen, D.C. Koopman, C.C. Herman, J.B. Pickett, J.R. Zamecni, Electron equivalents redox model for high level waste vitrification, in: Symposium on Waste Management Technologies in Ceramic and Nuclear Industries, Westinghouse Savannah River Company Aiken, American Ceramic Society, 2003.

[85] Karamanov, A. Pisciella, P. Cantalini, C. & Pelino, M. Influence of Fe3+/Fe2+ ratio on the crystallization of iron-rich glasses made with industrial wastes. 57, 3153–3157 (2000).

[86] A.A. Kruger, K.S. Matlack, W. Gong, I.L. Pegg, Small-Scale Melter Testing With LAW Simulants to Assess the Impact of Higher Temeprature Melter Operations ORP-51809, Office of River Protection, WA, (United States), 2012. VSL-04R4980-1.

[87] K.S. Matlack, I.S. Muller, W. Gong, I.L. Pegg, A.A. Kruger, Final Report - Duramelter 100 Tests to Support LAW Glass Formulation Correlation Development, Catholic University of America, DC, (United States), 2006. VSL-06R6480-1.

[88] D.F. Bickford, P. Hrma, B.W. Bowan, Control of radioactive waste glass melters: II, residence time and melt rate limitations, J. Am. Ceram. Soc. 73 (1990) 2903–2915.

[89] Smith, P.A. Vienna, J.D. & Merz, M.D. NCAW feed chemistry: effect of starting chemistry on melter offgas and iron redox, Richland, WA, (United States) PNL-10517. (1996).

[90] Weimers, K.D. The effect of HWVP feed nitrate and carbonate content on glass redox adjustment. Richland, WA, (United States) PNNL-11044 (1996).

[91] H.D. Schreiber, M. Todd Coolbaugh, Solvations of redox ions in glass-forming silicate melts, J. Non Cryst. Solids 181 (1995) 225–230.

[92] H.D. Schreiber, B.K. Kochanowski, C.W. Schreiber, A.B. Morgan, M.T. Coolbaugh, T.G. Dunlap, Compositional dependence of redox equilibria in sodium silicate glasses, J. Non Cryst. Solids 177 (1994) 340–346.

[93] K.S. Ranasinghe, R. Singh, D.E. Day, K. Attenkofer, E. Stavitski, L.A. Quinn, D. Patterson, A. Duenas, Evidence of the coexistence of multivalence cerium oxide nano-particles in a sodium borate glass, J. Non Cryst. Solids 515 (2019) 75–81.

[94] C. Lopez, X. Deschanels, J.M. Bart, C. Levrau, Solubility of plutonium surrogates in nuclear glasses, Sci. Res. Back-end Fuel Cycle 21. Century (2003) 1–5.

[95] H.D. Schreiber, S.J. Kozak, R.C. Merkel, G.B. Balazs, P.W. Jones, Redox equilibria and kinetics of iron in a borosilicate glass-forming melt, J. Non Cryst. Solids 84 (1986) 186–195.

[96] H.D. Schreiber, A.L Hockman, Redox chemistry in candidate glasses for nuclear waste immobilization, J. Am. Ceram. Soc. 70 (1987) 591–594.

[97] Aman, S.P Singh, Role of tin as a reducing agent in iron containing heat absorbing soda-magnesia-lime-silica glass, Bull. Mater. Sci. 27 (2004) 537–541.

[98] Y.A. Guloyan, Conditions for producing amber and brown glass, Glas. Ceram. (English Transl. Steklo i Keramika) 62 (2005) 301–303.

[99] S. Körner, K. Reinhardt, U. Partsch, M. Eberstein, Influence of oxygen micro atmosphere during contact formation, Energy Procedia 55 (2014) 688–692.

[100] C.M. Jantzen, Development of Glass Matrices For High Level Radioactive wastes. in Handbook of Advanced Radioactive Waste Conditioning Technologies, Woodhead Publishing Limited, 2011, pp. 230–292.